

Electronic Supplementary Data

Facile Synthesis of SnO₂-PbS Nanocomposites with Controlled Structure for Applications in Photocatalysis

Arik Kar,¹ Sumanta Sain,² David Rossouw,^{1,3} Benjamin R. Knappett,¹ Swapan Kumar Pradhan²
and Andrew E. H. Wheatley^{1*}

¹*Department of Chemistry, University of Cambridge, Lensfield Road, Cambridge, CB2 1EW, UK*

²*Materials Science Division, Department of Physics, The University of Burdwan, Golapbag,
Burdwan, West Bengal-713 104, India.*

³*Department of Materials Science and Engineering, Brockhouse Institute for Materials
Research and Canadian Centre for Electron Microscopy, McMaster University, Hamilton,
Ontario, L8S 4L8, Canada.*

PbS nanocube (NC) preparation

Pb(NO₃)₂ (0.033 g, 0.1 mmol) was dissolved in water (25 ml) at room temperature under Ar. over 30 mins. the temperature of the solution was raised to 50 °C. Na₂S·9H₂O (0.024 g, 0.1 mmol) was dissolved in water (25 ml) and the resulting solution added dropwise to that of Pb(NO₃)₂ by syringe. A black colloidal suspension slowly began to form and was stirred vigorously at 50 °C for 2 hrs. After this, the black colloidal suspension was cooled to room temperature. The precipitate was collected by centrifugation and washed using absolute ethanol (5x25 ml). The obtained black precipitate was vacuum dried in an oven at 70 °C for 2 hours to obtain the final product as black powder.

Rietveld analysis

One of great triumphs of Rietveld's powder structure refinement process¹⁻⁴ for x-ray powder diffraction (XRD) data is to characterize both structure and micro/nano-structure as well as achieving quantitative phase estimation in multiphase materials. The method involves simulation by the Marquardt least-square refinement procedure (in terms of an analytical function) of the experimental XRD pattern, a process that allows the treatment of different structural/microstructural parameters of each individual phase present in the sample. Since Bragg reflections always contribute to the intensity (y_i) at any arbitrary point,⁵ the calculated intensities (y_{ci}) can be described according to:

$$y_{ci} = S \sum_k L_k |F_k|^2 \Phi(2\theta_i - 2\theta_k) P_k A + y_{bi} \quad (1)$$

where S is the scale factor, k represents the Miller indices (h,k,l) for a Bragg reflection, L_k represents the Lorentz polarization and multiplicity factors, Φ is the reflection profile function, P_k is the preferred orientation function, F_k is the structure factor for the kth Bragg reflection, A is the absorption function, and y_{bi} is the background intensity of the ith step. In the present work, Rietveld's software Materials Analysis Using Diffraction, MAUD (version 2.33)⁶ was used to simultaneously refine the different structural and microstructural parameters governing equation (1). These included background polynomial coefficients (of degree four in the present case), atomic coordinates, lattice parameters, phase volume, peak shape parameters, etc. The process of refinement was an iterative method and the probable value of different parameters depended on

the goodness of fit (GoF).¹⁻⁴ This can be expressed as the ratio of reliable index parameters R_{wp}

$$R_{wp} = \left[\frac{\sum_i w_i (Y_{io} - Y_{ic})^2}{\sum_i w_i Y_{io}^2} \right]^{\frac{1}{2}}$$

to R_{exp} , where weighted residual error

and expected residual error

$$R_{exp} = \left[\frac{(N - P)}{\sum_i w_i Y_{io}^2} \right]^{\frac{1}{2}}$$

. Here, w_i is the statistical weight, Y_{io} and Y_{ic} are the observed and calculated X-ray diffraction intensity, N is the weight and number of experimental observations and P is the number of fitting parameters. In the present work the value of GoF lay between 1.1 and 1.2 and this suggested a good quality refinement. In the present case we used the following pseudo-Voigt (pV) analytical function to fit the experimental XRD data:⁷

$$pV(2\theta) = \sum_{\alpha_1 \alpha_2} I_{nt} [(1 - \eta)(1 + S^2)^{-1} + \eta \exp(-\ln 2 \times S^2)] \quad (2)$$

where $S = \frac{(2\theta - 2\theta_0)}{HWHM}$ and I_{nt} represents scale parameter of the pV function, η is the Gaussianity of the peak, HWHM is the half-width-at-half-maximum of the peak, θ_0 is the exact Bragg angle for $K\alpha_1$ peak. The shape parameter HWHM and the Gaussianity of the true line broadening function at different scattering angles can be calculated using the crystallite size (D) and microstrain ($\langle \varepsilon^2 \rangle^{1/2}$) values of a sample as the fitting parameters.⁷⁻⁸ The full-width-at-half-maximum (FWHM) H can then be modeled as:⁹

$$H^2 = U \tan^2 \theta + V \tan \theta + W \quad (3)$$

where U, V and W are refinable parameters.

Phase identification by XRD

Figure S1 shows the XRD pattern for PbS NCs, reflections being indexed with cubic PbS (ICSD code 62190, space group, $Fm\bar{3}m$, $a = 5.9143 \text{ \AA}$) and the peaks being less broad than those of the

SnO₂ NPs. Peak broadening in PbS is, however, not equal, suggesting anisotropy. Again, a lack of uniformity in the peak widths indicates particle anisotropy, and the contribution of particle size and r.m.s lattice strain to peak broadening as a function of crystallographic direction has been determined (see Table S1 below). Planar defects (faults) such as intrinsic (α'), extrinsic (α'') and twin (β) faults have been estimated both qualitatively and quantitatively for PbS from the Rietveld analysis. Quantitative estimation of planar defects is expressed through stacking fault probabilities in 10^4 lattice planes and is shown in Table S1.

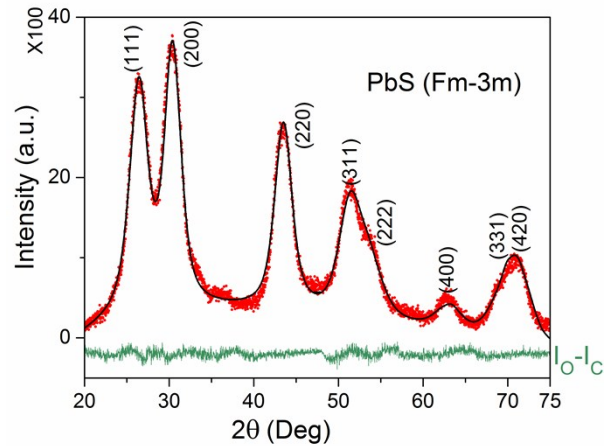


Figure S1 Observed (I_O , red dots) and simulated (I_C , black line) XRD patterns (indexed) of PbS NCs. The green line represents $I_O - I_C$.

Table S1 Microstructural parameters obtained for PbS NCs.

Lattice parameter (Å)	Anisotropic particle size (nm)	Direction (plane)	Anisotropic lattice strain	Planar defects(10^{-4})		
				Intrinsic (α')	Extrinsic (α'')	Twin (β)
5.9163	4.92	111	0.0139	0.4148	15.00	1.6838
	6.06	200	0.0136			
	5.97	220	0.0096			
	5.83	311	0.0144			
	4.92	222	0.0139			
	6.06	400	0.0136			

5.80	331	0.0129
6.12	420	0.0122

Figure S2 shows evidence for the presence of stacking faults obtained by Rietveld analysis. Data reveal that the (111) plane shifts towards high scattering angle whereas the (200) plane shifts towards low scattering angle. Such behavior is explained by the cumulative effects of stacking fault probabilities and long range residual stresses;¹⁰ this has also been observed in CdZnS quantum dots.¹¹

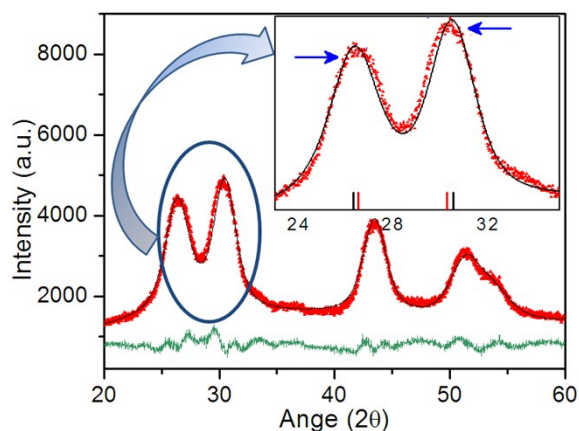


Figure S2 Shift in nanocube (red) and reference (ICSD database no. 62190, black) XRD maxima for PbS. Arrows show direction of peak position shift (inset).

Atomic structures and modeling

To study the atomic arrangements in SnO₂ nanoparticles and PbS nanocubes atomic modeling of tetragonal SnO₂ and cubic PbS phase was undertaken. Atomic structures of tetragonal SnO₂ nanoparticles are shown in Figure S3. In Figure S3a, SnO₆ octahedra are shown and their position within a unit cell is shown in Figure S3b, the fractional coordinates of Sn and O atoms being (0, 0, 0) and (0.367, 0.242, 0) respectively. An isolated octahedron is shown in Figure S3c. Evidencing the fact that the SnO₆ octahedra are tilted and exhibit John-Teller distortions by virtue of the deviation in lattice parameters and fractional coordinates of O atoms from those of the bulk (powder) SnO₂ (ICSD database no. 154960). All Sn–O and Sn···Sn distances in bulk

SnO₂ are 2.05 Å and 3.18 Å respectively. In contrast, in the case of SnO₂ nanoparticles Sn–O bond lengths are exhibit two distinct values: 2.07 Å and 2.09 Å. Hence, the length of each of the equatorial Sn–O bonds (as depicted in Figure S3d) is 2.09 Å whilst that of each axial Sn–O bond is 2.07 Å. The lengths of all Sn···Sn non-bonding distances have also increased to 3.26 Å. However, unlike the Sn–O bonds, all the Sn···Sn distances are computed to be equal in SnO₂ nanoparticles.

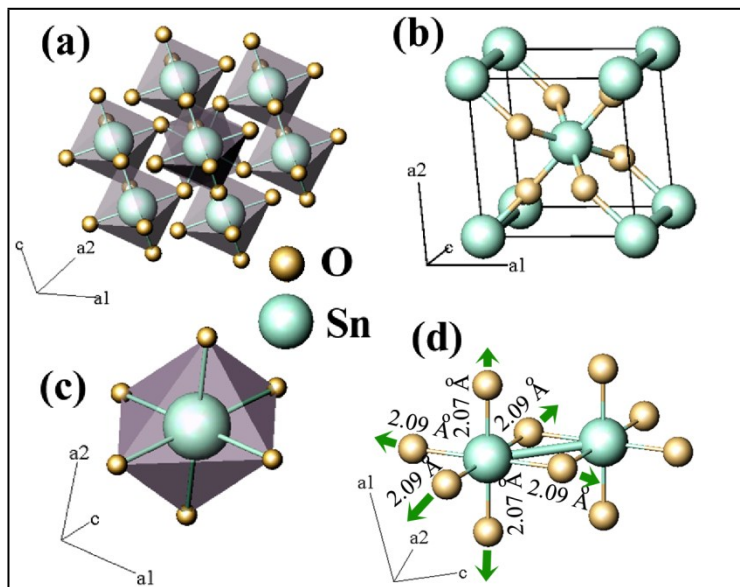


Figure S3 Atomic arrangements of (a) tetragonal SnO₂ nanoparticles forming octahedra, (b) the corresponding unit cell, (c) an isolated octahedron and (d) coupled octahedra.

Figure S4a shows the atomic arrangements in the PbS₆ octahedral network that forms the basis of a face centred cubic (fcc) PbS nanocube. A unit cell of the PbS lattice with a lattice parameter of 5.9163 Å is shown in Figure S4b, with the Pb atom remaining at the face centred position ($\frac{1}{2}$, $\frac{1}{2}$, $\frac{1}{2}$) and the S atom remaining at (0, 0, 0) position. An isolated octahedron is shown in Figure S4c. Pb–S bond lengths in the PbS nanocubes are found to be 2.958 Å, which is marginally higher than those in bulk (powder) PbS (ICSD database no. 62190). The extension in the Pb–S bond length is associated with the expansion of lattice parameter on the nanoscale. The result is that the octahedral void space in a PbS nanocube is also greater than that in the bulk PbS lattice.

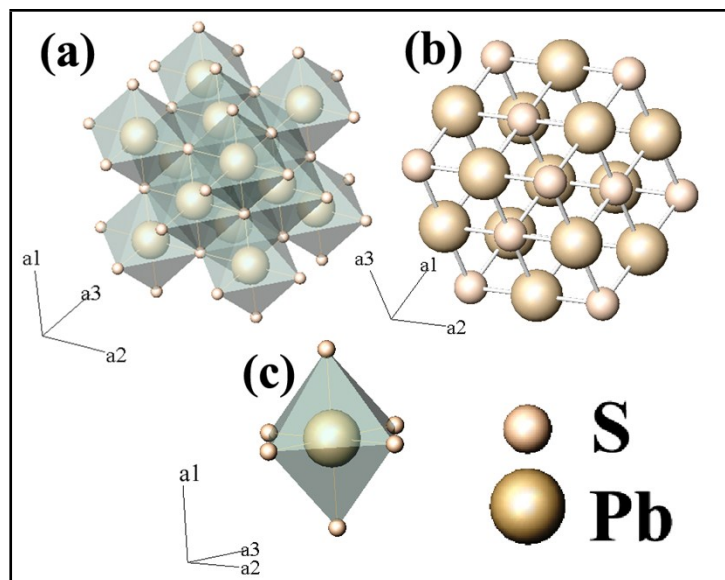


Figure S4 (a) Atomic structure, (b) unit cell and (c) an isolated octahedron of PbS in a nanocube.

The atomic structures of SnO₂ and PbS components in a SnO₂-PbS nanocomposite are shown in Figure S5. In Figure S5a, SnO₆ octahedra are shown. In contrast to those in Figure S3, these octahedra are not tilted and are free from Jahn-Teller distortion. The fractional coordinates for the Sn and O atoms are (0, 0, 0) and (0.346, 0.184, 0) respectively. An isolated octahedron is shown in Figure S5b. All Sn–O bond lengths are, at 2.33 Å, equal and extended relative to those in nanoparticulate SnO₂ (*cf.* Figure S3d). On the contrary, Sn···Sn distances are, at 3.22 Å, equal and relatively shortened (*cf.* Figure S3d). The atomic arrangement in the PbS lattice consists of PbS₆ octahedra and these are shown in Figure S5c. An isolated PbS octahedron is shown in Figure S5d. This reveals Pb–S bond lengths in the SnO₂-PbS nanocomposite that are equal at 2.99 Å. This value is greater than that noted for both bulk PbS and PbS nanocubes.

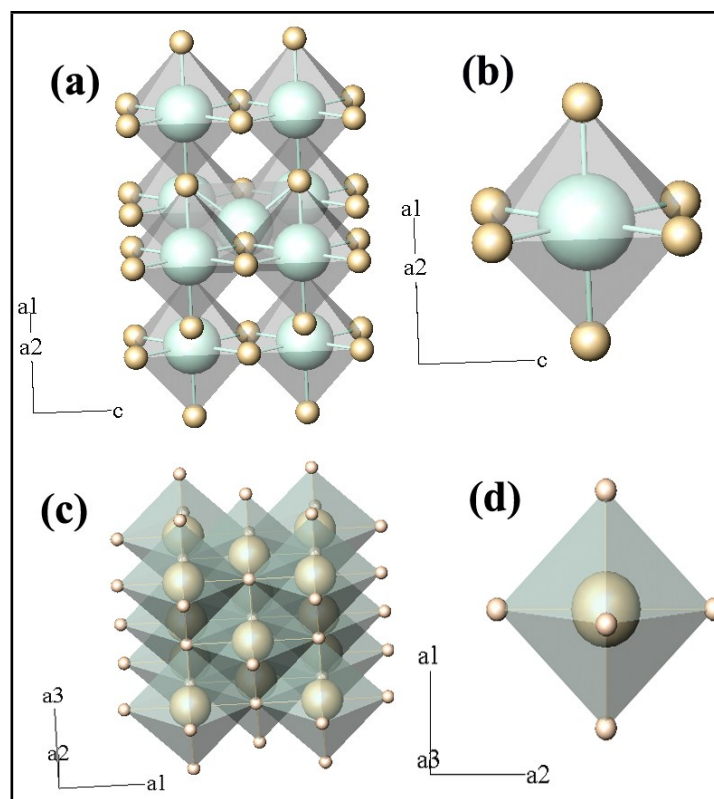


Figure S5 (a) Atomic structure of SnO₂ nanocrystals, (b) an isolated SnO₂ octahedron in a SnO₂-PbS nanocomposite, (c) the atomic structure of PbS nanocubes, and (d) an isolated PbS octahedron in a SnO₂-PbS nanocomposite.

TEM analysis

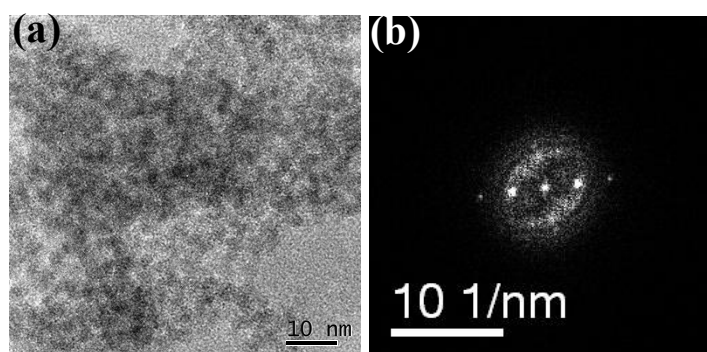


Figure S6 (a) Representative TEM image of SnO₂ nanoparticles and (b) FFT pattern of a single SnO₂ nanoparticle (marked by the red circle in Figure 4 in the main manuscript) showing prominent reflections corresponding to a lattice spacing of 3.30 Å.

Figure S7a confirms the formation of *ca.* 22.5 ± 2.9 nm wide PbS NCs that result when the synthetic route to PbS employed throughout this paper is attempted in the absence of preformed SnO₂ NPs. Figure S7b reveals lattice fringes ($d = 0.30 \pm 0.02$ nm) for the (200) lattice planes in nanoscopic PbS.¹²

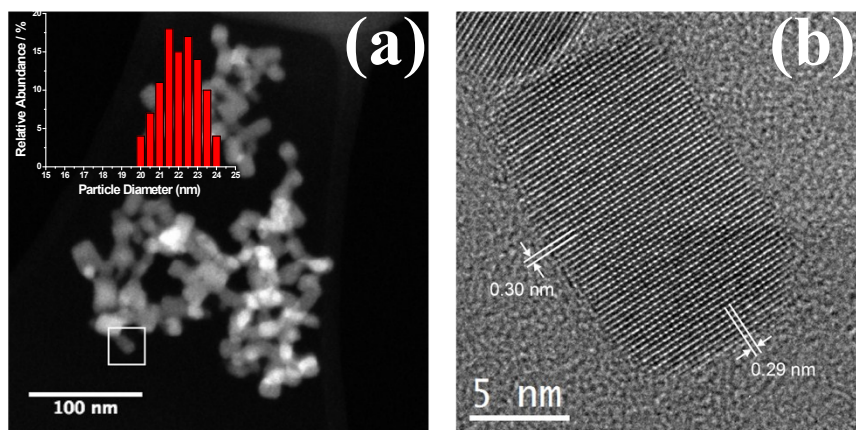


Figure S7 (a) Dark field TEM image of PbS NCs and the particle size distribution for the sample (inset) and (b) a representative HRTEM image of a PbS NCs indicating the measured distance between the lattice planes.

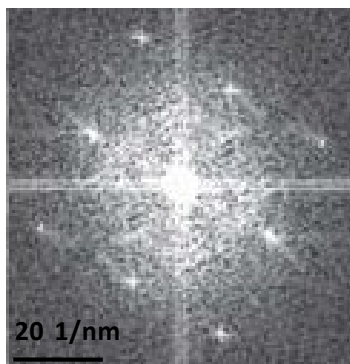


Figure S8 The FFT pattern obtained from the PbS nanocube shown in Figure S7b.

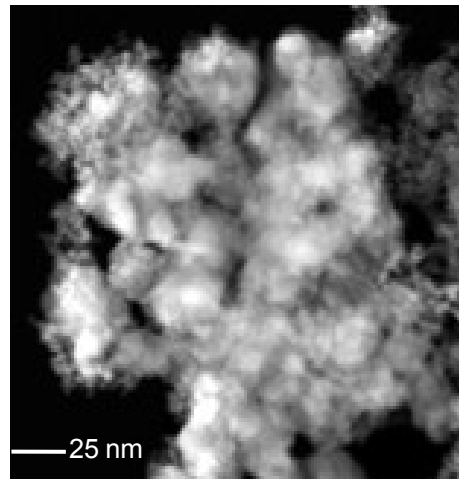


Figure S9 A representative dark field STEM image of the product obtained by introducing PbS to surface-modified SnO₂ nanoparticles.

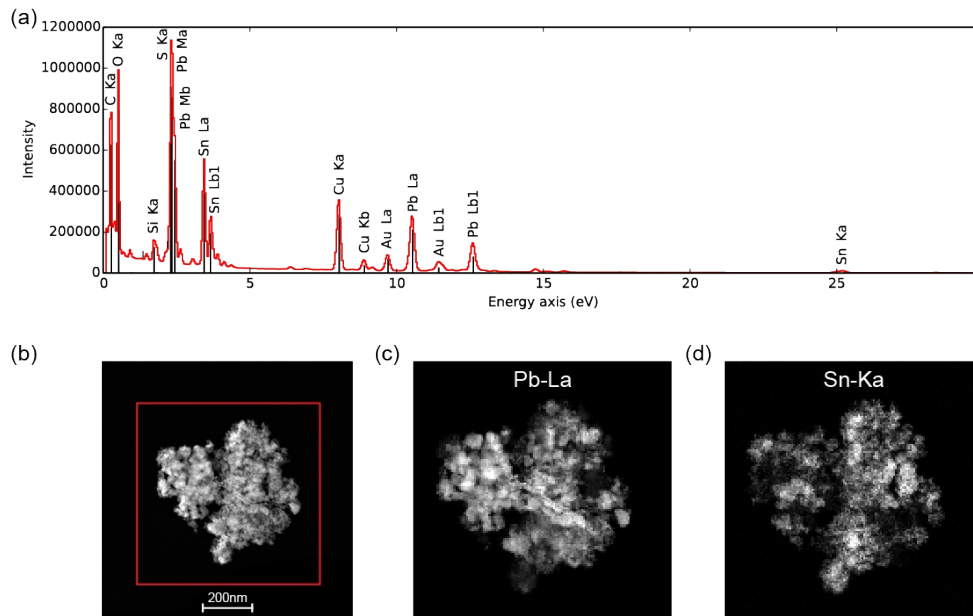


Figure S10 (a) Integrated X-ray signal from an EDX spectrum image (Au and Cu attributable to grid and sample holder) obtained from a region enclosing (b) a representative product agglomerate, imaged by HAADF-STEM, obtained by attempting the synthesis of PbS NCs in the presence of surface-modified SnO₂ NPs. (c) and (d) Spatial distribution of the corresponding Pb-Lα and Sn-Kα emissions.

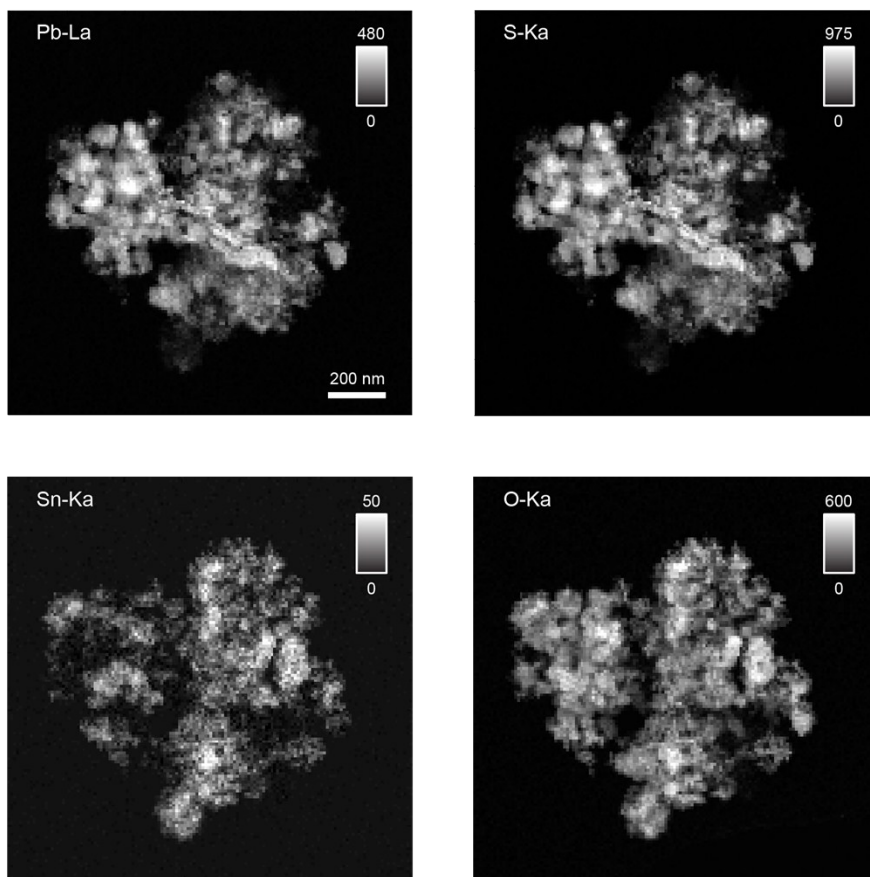


Figure S11 EDX analysis of SnO₂-PbS reveals the spatial distributions of lead (Pb-L α line), tin (Sn-K α line), sulfur (S-K α line) and oxygen (O-K α line) and suggests nanocomposite formation.

Independent component analysis

STEM-HAADF imaging and EDX spectrum imaging of the SnO₂-PbS system revealed elemental Pb, Sn, O, S X-ray peaks originating from the sample, and Au and Cu peaks attributable to the 3 mm Au-Cu TEM support grid. The spatial distribution of the other elements suggested nanocomposite formation and this was explored using principle component analysis (PCA) and independent component analysis (ICA) of EDX spectrum images (SIs). The EDX SI data for a representative agglomerate was processed using machine learning methods implemented in HyperSpy.¹³ Results are summarized in the paper (Figure 5). The spectral dimension in the dataset was binned by four from 5 eV/channel to 20 eV/channel in order to

increase the number of counts per channel, after which a linear variance-stabilizing transformation for Poisson statistics¹⁴ was applied. PCA was performed to identify strong spectral patterns in the SI dataset. The first five principal components exhibited significantly greater variance than the remaining components, and were retained for ICA. The first derivative of each retained PCA spectral component was calculated and ICA was implemented to maximize their statistical independence. The independent component vectors (IC#0-4) and their weightings are displayed as spectra and maps respectively in the paper in Figure 5.

Raman spectroscopy

Figure S12 shows the Raman spectrum of PbS NCs at room temperature. It contains bands at 429 cm^{-1} , 602 cm^{-1} and 967 cm^{-1} . Generally, crystalline semiconductors or insulators reveal Raman shifts attributable to longitudinal optical (LO) modes, while other modes such as the transverse optical (TO) and the surface phonon (SP) tend not to be seen due to a combination of symmetry restrictions and low intensity.¹⁵ The 967 cm^{-1} band may therefore be attributed to sulfates present in the sample on account of laser-induced degradation. This explains why the XRD pattern (see above) demonstrates cubic PbS but not PbSO_4 .¹² The peaks at 429 cm^{-1} and 602 cm^{-1} represent first and second overtones of the fundamental LO phonon mode (2LO and 3LO, respectively).¹⁶

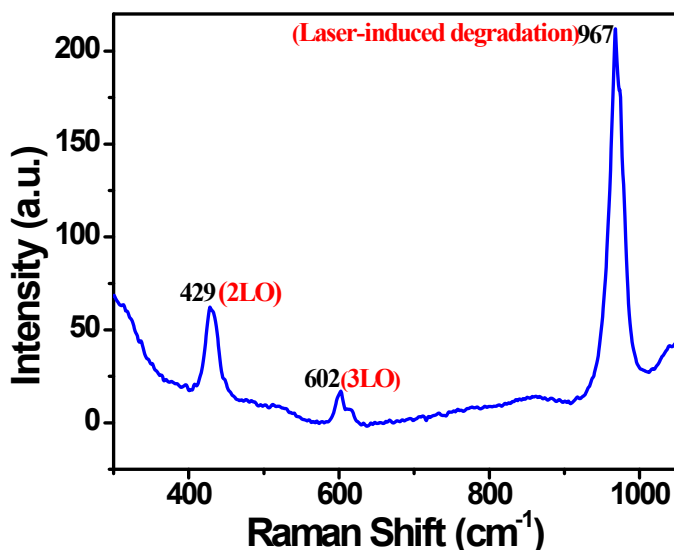


Figure S12 Room temperature Raman spectrum of PbS nanocubes.

X-ray photoelectron spectroscopy (XPS)

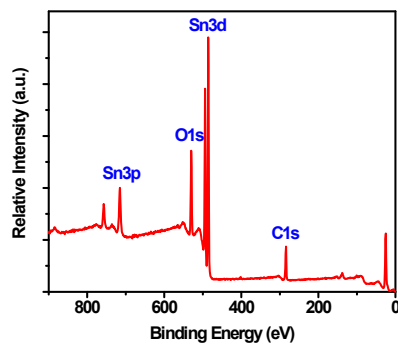


Figure S13 XPS survey spectrum for SnO₂ nanoparticles. The C1s peak can be tentatively attributed to surface carbon contamination

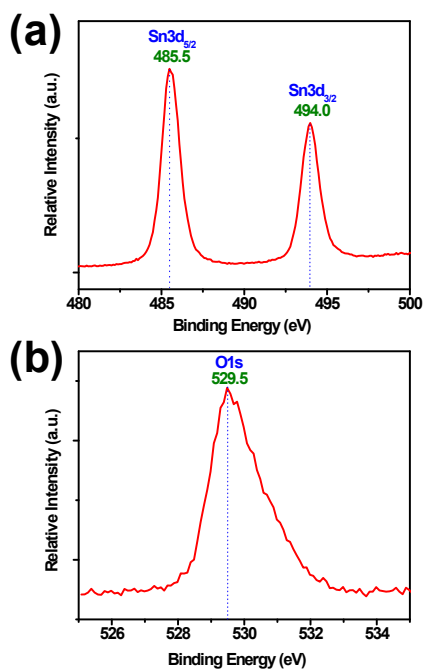


Figure S14 XPS data for SnO₂ nanoparticles: (a) binding energy spectrum for Sn3d;¹² (b) the binding energy spectrum for O1s can be attributed to the lattice oxygen in SnO₂.¹⁷

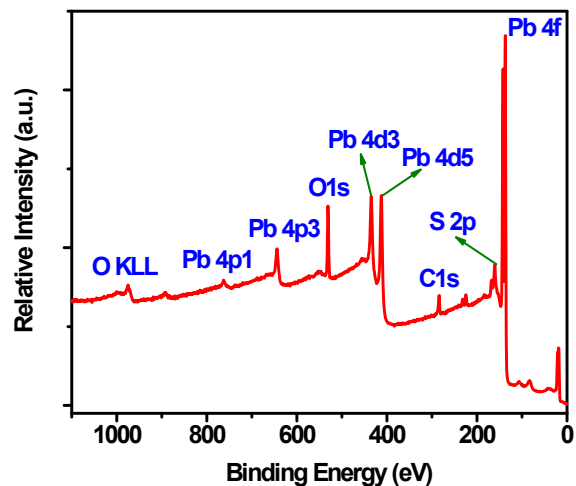


Figure S15 XPS survey spectrum for PbS nanocubes. The C1s and O1s peaks can be tentatively attributed to adsorbed gaseous molecules owing to the high surface-to-volume ratio of the PbS NCs.¹⁸

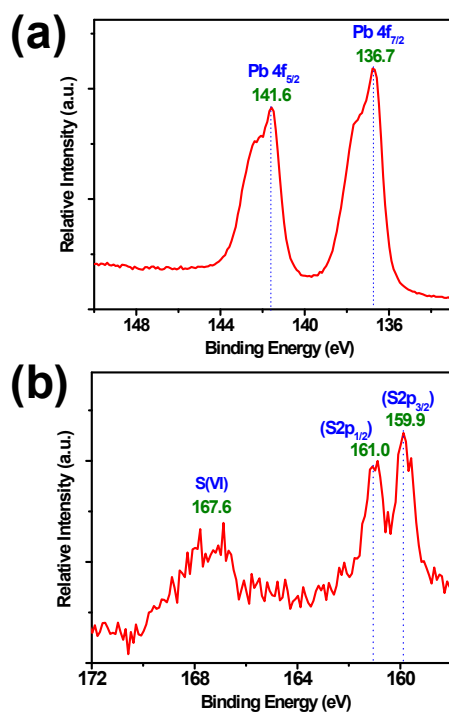


Figure S16 XPS data for PbS nanocubes: (a) binding energy spectrum for Pb4f; (b) binding energy spectrum for S2p is attributable to S(VI).¹⁹

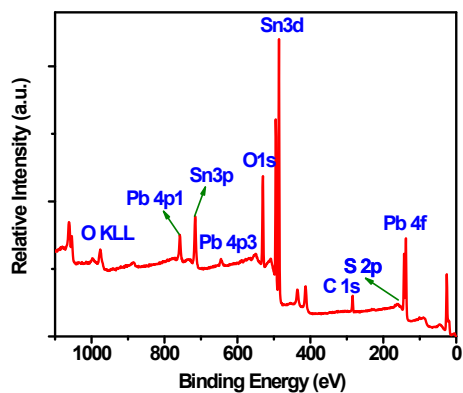


Figure S17 XPS survey spectrum for SnO₂-PbS nanocomposites. The C 1s peak can be tentatively attributed to adsorbed gas molecules and surface carbon contamination.^{18,20}

UV-Vis spectroscopy

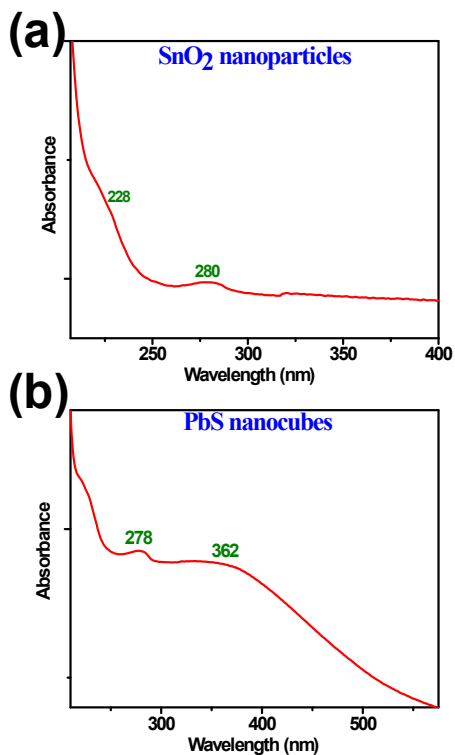


Figure S18 UV-Vis absorption spectra of (a) SnO₂ nanoparticles²¹ and (b) PbS nanocubes^{22,23} in aqueous solution.

Photocatalytic experiments

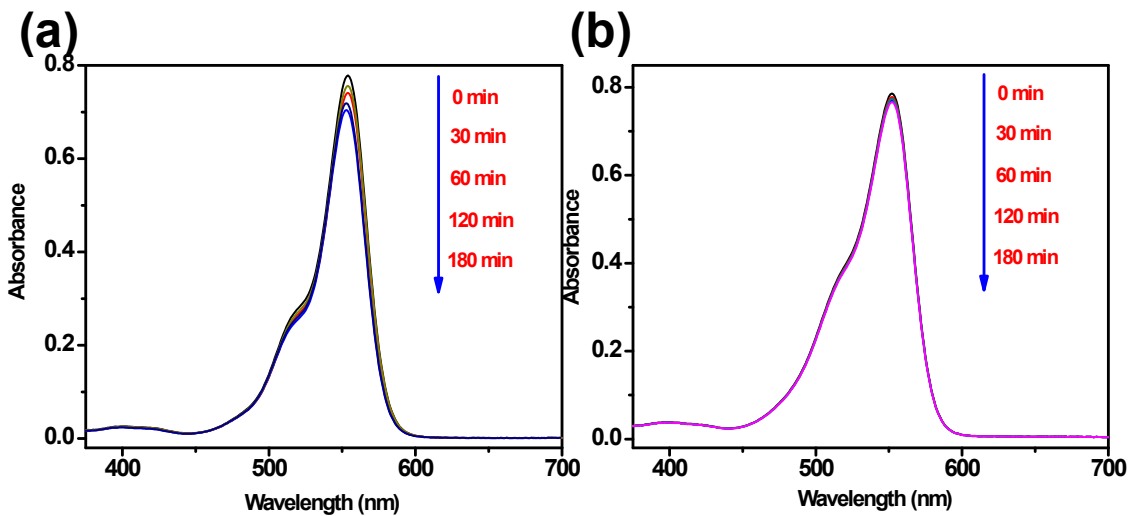


Figure S19 Spectral changes for the $\lambda_{\max} = 555$ nm absorption of Rhodamine B (a) irradiating in the absence of nanoparticulate photocatalyst and (b) in the presence of nanocomposite photocatalyst but without irradiation.

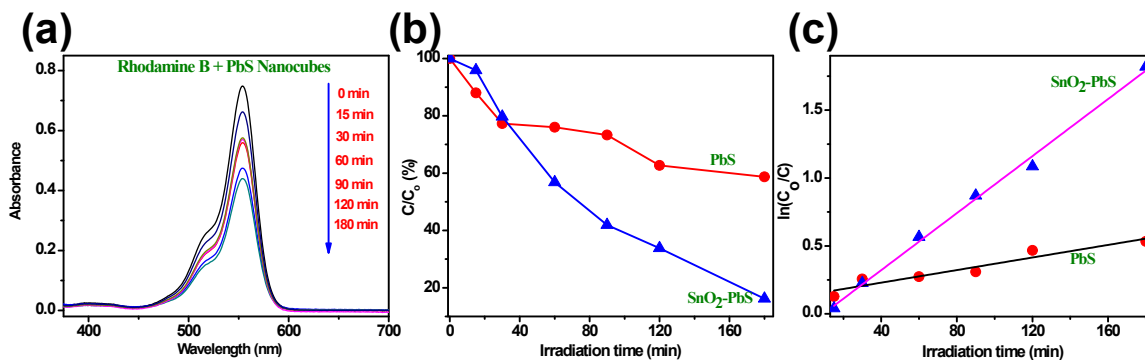


Figure S20 Photocatalytic data for PbS NCs (5.0 mg of catalyst). RhB absorption maximum at *ca.* 555 nm (a), and plots of C/C_0 (%) for RhB as a function of irradiation time in the presence of PbS NCs and $\text{SnO}_2\text{-PbS}$ nanocomposites (b) and $\ln(C_0/C)$ as a function of irradiation time in the presence of PbS NCs and $\text{SnO}_2\text{-PbS}$ nanocomposites (c) (C_0 and C are the concentrations of dye before and after irradiation, respectively). The apparent rate constant for pure PbS NCs was determined to be $2.3 \times 10^{-3} \text{ min}^{-1}$.

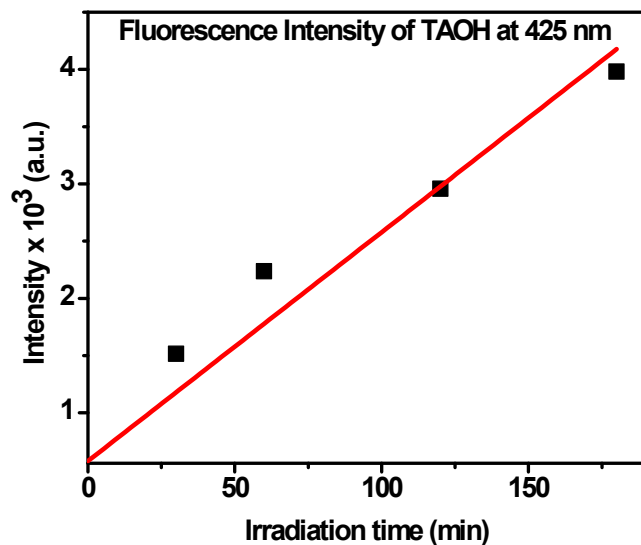


Figure S21 Fluorescence intensity at 425 nm against illumination time for TAOH.

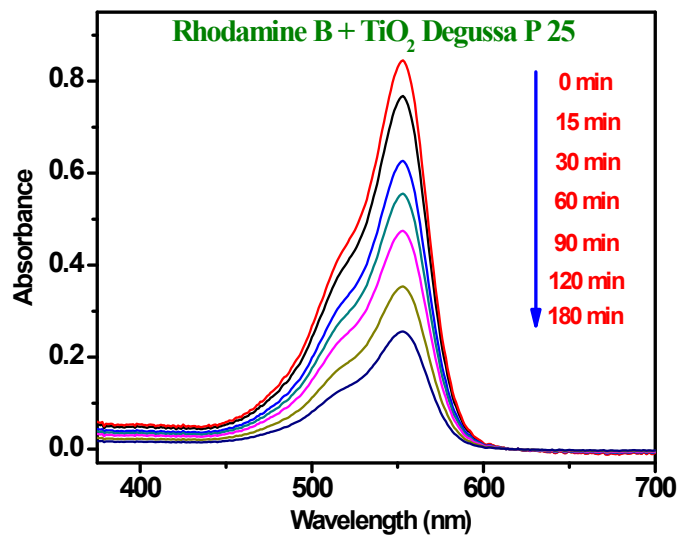


Figure S22 Absorption by aqueous Rhodamine B in the presence of standard photocatalyst TiO₂ Degussa P25 (5.0 mg).

BET surface area analysis

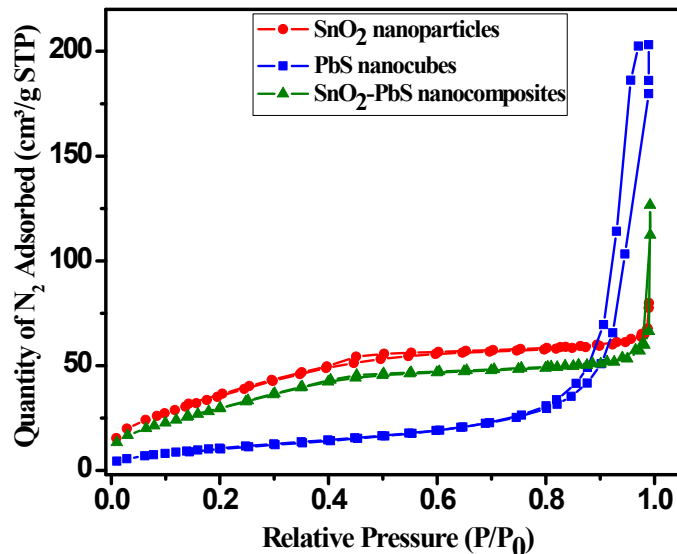


Figure S23 Nitrogen adsorption-desorption isotherms (P and P_0 are the equilibrium and the saturation pressures of N_2 at the temperature of adsorption) for SnO_2 nanoparticles, PbS nanocubes and SnO_2 -PbS nanocomposites. For PbS, $S_{BET} = 39.1641 \text{ m}^2\text{g}^{-1}$, pore vol. = 0.313853, mean pore size = 24.3725 nm.

References

1. H. M. Rietveld, *Acta Crystallogr.*, 1967, **22**, 151–152.
2. H. M. Rietveld, *J. Appl. Crystallogr.*, 1969, **2**, 65–71.
3. L. Lutterotti, P. Scardi and P. Maistrelli, *J. Appl. Crystallogr.*, 1992, **25**, 459–462.
4. R. A. Young and D. B. Willes, *J. Appl. Crystallogr.*, 1982, **15**, 430–438.
5. R. A. Young, (1996) *The Rietveld Method* Oxford University Press Inc, New York.
6. L. Lutterotti, Program Maud (version 2.33) Online <http://maud.radiographema.com/>
7. L. Lutterotti and P. Scardi, *J. Appl. Crystallogr.*, 1990, **23**, 246–252.
8. A. Chanda and M. De, *J. Alloys Comp.*, 2000, **313**, 104–114.
9. G. Caglioti, A. Paoletti, F. P. Ricci, (1958) *Nucl Instrum Methods* 3:223–228.
10. B. E. Warren, 1969 *X-ray Diffraction*. Addison-Wesley, Reading, MA; C. N. G. Wagner, 1966, *Local Atomic Arrangements Studied by X-ray Diffraction*. Gordon and Breach, New York.

11. S. Sain, A. Kar, A. Patra and S. K. Pradhan, *J. Nanopart. Res.*, 2014, **16**, 2673–2688.
12. H. Cao, G. Wang, S. Zhang and X. Zhang, *Nanotechnol.*, 2006, **17**, 3280–3287.
13. See <http://www.hyperspy.org>
14. M. R. Keenan and P. G. Kotula, *Surf. Interface Anal.*, 2004, **36**, 203–212.
15. K. K. Nanda, S. N. Sarangi, S. N. Sahu, S. K. Deb and S. N. Behera, *Physica B*, 1999, **262**, 31–39.
16. G. D. Smith, S. Firth, R. J. H. Clark and M. Cardona, *J. Appl. Phys.*, 2002, **92**, 4375–4380.
17. L. Cao, H. Wan, L. Huo and S. Hi, *J. Colloid Interface Sci.*, 2001, **244**, 97–101.
18. M. S. Bakshi, P. Thakur, S. Sachar, G. Kaur, T. S. Banipal, F. Possmayer and N. O. Petersen, *J. Phys. Chem. C*, 2007, **111**, 18087–18098.
19. S. Chen and W. Liu, *Mater. Chem. Phys.*, 2006, **98**, 183–189.
20. C. Wang, C. Shao, X. Zhang and Y. Liu, *Inorg. Chem.*, 2009, **48**, 7261–7268.
21. J. Kang, S. Tsunekawa and A. Kasuya, *Appl. Surf. Sci.*, 2001, **174**, 306–309.
22. S. Acharya, U. K. Gautam, T. Sasaki, Y. Bando, Y. Golan and K. Ariga, *J. Am. Chem. Soc.*, 2008, **130**, 4594–4595.
23. F. Li, X. Huang, T. Kong, X. Liu, Q. Qin and Z. Li, *J. Alloy. Comp.*, 2009, **485**, 554–560.